research papers

CrossMark

Correcting for surface topography in X-ray fluorescence imaging

E. C. Geil and R. E. Thorne*

Laboratory of Atomic and Solid State Physics, Cornell University, Ithaca, NY 14853, USA.
*E-mail: ret6@cornell.edu

Samples with non-planar surfaces present challenges for X-ray fluorescence imaging analysis. Here, approximations are derived to describe the modulation of fluorescence signals by surface angles and topography, and suggestions are made for reducing this effect. A correction procedure is developed that is effective for trace element analysis of samples having a uniform matrix, and requires only a fluorescence map from a single detector. This procedure is applied to fluorescence maps from an incised gypsum tablet.

Keywords: X-ray fluorescence; imaging; surface angle; surface orientation; topography.

1. Introduction

In synchrotron-based X-ray fluorescence imaging (XRFI), a small-diameter beam of synchrotron-generated X-ray radiation is scanned across the surface of an object. The fluorescence signal from each point is measured using an energy-dispersive detector, and then analyzed to yield a two-dimensional map of elemental concentrations across the object's surface (Rivers *et al.*, 1992; Mantler & Schreiner, 2000; Solé *et al.*, 2007). This technique can furnish important information about a wide range of objects, including biological specimens (Limburg *et al.*, 2007), mineral specimens (Lintern *et al.*, 2013), paintings (Dik *et al.*, 2008) and archaeological artifacts, including ancient documents on parchment and stone (Bergmann & Knox, 2009; Powers *et al.*, 2005, 2009).

Analysis of XRFI data is most straightforward for objects with flat surfaces. For objects with surface curvature or relief, such as vases or tablets with incised letters (Powers *et al.*, 2005, 2009), variations in local surface orientation relative to the incident X-ray beam modulate the intensity of X-ray fluorescence received at the detector (Bonizzoni *et al.*, 2006). These geometry-related intensity modulations cannot easily be distinguished from those due to variations in sample composition. The problem of quantitative X-ray fluorescence (XRF) analysis of objects with arbitrary geometries is difficult and often ill-posed (Urbach & de Bokx, 2001). Computationally intensive Monte Carlo methods (Scot *et al.*, 2007; Trojek *et al.*, 2010; Trojek & Wegrzynek, 2010; Trojek, 2011, 2012) have been successfully applied in some cases.

Here, we derive simple expressions for the variation of fluorescence intensity with surface orientation, and discuss a procedure to correct fluorescence maps for the effects of surface relief. Although the necessary assumptions about sample surface relief and composition and about measurement geometry are fairly restrictive, the analysis is still useful for many real-world samples, as we will illustrate.

2. Variation of detected fluorescence intensity with surface and detector angles

To analyze the effect of surface relief, we make the following simplifying assumptions:

(i) Variations in surface orientation and sample composition are small on the scales of the incident X-ray beam width ($\sim$1 µm–1 mm) and penetration depth ($\sim$500 µm), respectively.

(ii) The detector is far from the surface, so that differences in path length and angle from various points in the X-ray illuminated and fluorescing sample volume to the detector can be neglected, and integration over the detector's solid angle is unnecessary.

(iii) The sample's surface relief and the sample and detector orientations are such that there is an unobstructed path from the incident beam's interaction point to the detector for all points on the sample surface, *i.e.* the path to the detector from one point on the sample surface is not blocked by another part of the surface.

(iv) There is no secondary fluorescence.

As illustrated in Fig. 1 (left), we choose coordinates so that the beam intersects the surface at the origin, and define unit vectors **b** along the incident X-ray beam direction, **n** along the surface normal at the incident beam's interaction point, and **d** from the interaction point to the detector.

The intensity of the fluorescence signal at the detector is

$$I = \lambda \int_0^\infty \exp(-\mu_i s_i) \exp(-\mu_f s_f)\, ds_i, \qquad (1)$$

where λ is a constant involving the fluorescence yield and detector solid angle; $\mu_i = \mu(E_i)$ [$\mu_f = \mu(E_f)$] is the sample attenuation coefficient at the incident [fluorescent] energy, and s_i [s_f] is the length of the line from the sample surface to the interaction point along the beam direction [detector direction], as shown in Fig. 1 (right).
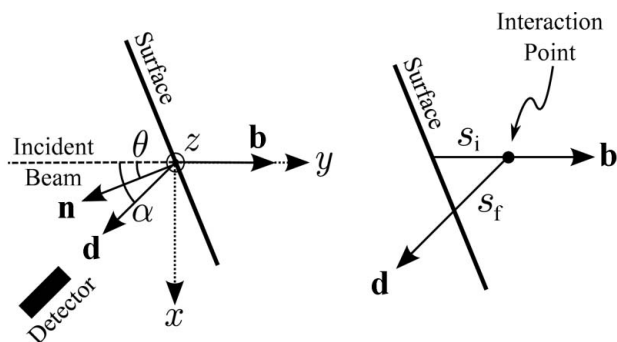
Figure 1
Measurement geometry for calculation of how the measured XRF intensity varies with surface orientation. The xy plane is defined by the incident X-ray beam direction and detector. Left: $\mathbf{b}$, $\mathbf{d}$, $\mathbf{n}$ are the incident beam direction, the direction from the interaction point to the detector, and the surface normal direction (which in general projects out of the xy plane), respectively. The rotations of $\mathbf{n}$ and $\mathbf{d}$ around the z axis (with respect to $-\mathbf{b}$) are given by θ and α, respectively. Right: expanded view of the region around the interaction point. The incident beam travels a distance s_i from the surface to the interaction point, and the fluorescent photons travel a distance s_f from the interaction point to the surface.

To determine s_f, note that the interaction point is located at $s_i\mathbf{b}$, and that the vector $s_i\mathbf{b} + s_f\mathbf{d}$ must lie in the surface plane. The equation of the surface is $\mathbf{n} \cdot \mathbf{r} = 0$, so that

$$\mathbf{n} \cdot (s_i\mathbf{b} + s_f\mathbf{d}) = 0.$$

Thus,

$$s_f = -\frac{\mathbf{b} \cdot \mathbf{n}}{\mathbf{d} \cdot \mathbf{n}} s_i \equiv k s_i, \tag{2}$$

where k is a geometrical factor. (Note that s_f is negative or fails to exist when the surface is angled away from the detector.) Then,

$$I = \lambda \int_0^\infty \exp\left[-(\mu_i + k\mu_f)s_i\right] ds_i$$
$$= \lambda/(\mu_i + k\mu_f). \tag{3}$$

In our coordinate system the beam points along the $+y$ direction ($\mathbf{b} = \mathbf{y}$), and the detector lies in the xy (horizontal) plane, making an angle α with $-\mathbf{y}$. Then, if $\mathbf{n} = (n_x, n_y, n_z)$ and $\mathbf{d} = (\sin\alpha, -\cos\alpha, 0)$,

$$k = -\frac{\mathbf{b} \cdot \mathbf{n}}{\mathbf{d} \cdot \mathbf{n}} = \frac{-n_y}{n_x \sin\alpha - n_y \cos\alpha}$$
$$= (\cos\alpha + \tan\theta \sin\alpha)^{-1}, \tag{4}$$

where θ is the rotation of the surface normal around the z axis; $\theta = 0$ for a surface parallel to the xz plane. Finally, we have

$$I(\theta) \propto \frac{1}{1 + (\mu_f/\mu_i)(\cos\alpha + \tan\theta \sin\alpha)^{-1}}. \tag{5}$$

Fig. 2 shows $I(\theta)$ *versus* surface orientation angle θ at several detector angles α calculated using equation (5) and $\mu_f/\mu_i = 14$ (appropriate for Ca fluorescence in a calcite matrix, with an incident energy of 17 keV).
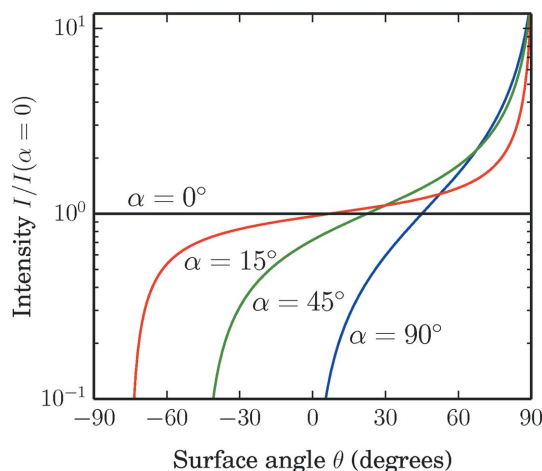

Figure 2
Variation of detected fluorescence intensity with surface angle θ as given by equation (5), with $\mu_f/\mu_i = 14$ and four detector angles α.

The above calculation leads to several observations. One, changes in the surface orientation θ result in changes in the detected fluorescence intensity and thus, if no correction is performed, in *apparent* changes in elemental composition (Fig. 3). The magnitude of this intensity variation with θ increases with increasing μ_f/μ_i, and so is often most apparent for low-Z elements, which have relatively small mass absorption coefficients μ_i, and for which μ_f at the relatively low energy of their K_α fluorescence is relatively large.

Two, under the given approximations, rotations of the surface normal out of the xy plane (for the polar coordinate φ within $\pm 90°$) do not change θ and the detected fluorescence intensity. Thus, whenever possible, objects should be mounted so that their dominant surface curvature runs perpendicular to the detector–incident-beam (xy) plane. For instance, mounting a cylindrical sample with its axis in the xy plane avoids position-dependent modulation of the fluorescence intensities.

Finally, the angle effect vanishes as the detector position approaches the incident beam, and is maximal when the detector is perpendicular to the beam. For polarized incident
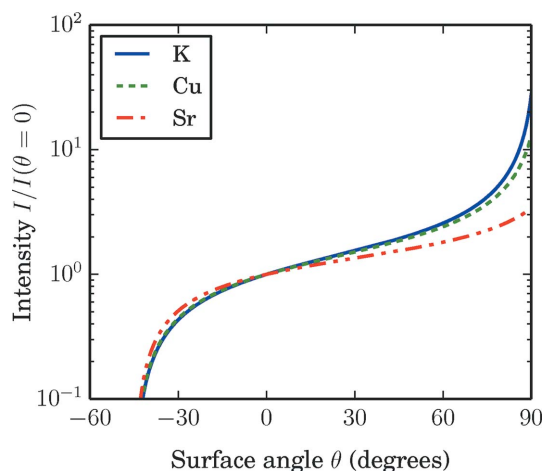

Figure 3
Variation of detected fluorescence intensity with surface angle θ for the K-$K_{\alpha1}$, Cu-$K_{\alpha1}$ and Sr-$K_{\alpha1}$ lines, in a $CaCO_3$ matrix, with incident beam energy 17 keV and detector angle $\alpha = 45°$.

radiation (*e.g.* synchrotron radiation), Compton scattering is greatly reduced when the detector is perpendicular to the beam, in the plane of polarization (Dzubay *et al.*, 1974). To minimize Compton background, typical XRF configurations place the detector at $\alpha = 90°$ and the sample normal at $\theta = 45°$. However, for samples with appreciable surface relief, a better approach is to orient the sample's 'mean' normal in the $-\mathbf{y}$ direction, and to set the detector at as small an angle α as practicable (typically about 45°). The very high counting rates possible using modern detectors make the Compton background less problematic.

Orienting the sample's mean normal and the translation stage's normal in the $-\mathbf{y}$ direction (so that translations occur in the xz plane) solves another problem too: if the stage is at any other angle, sample topography will vary the interaction point of the beam in stage xz coordinates, and therefore in the *image* coordinates. This distorts the images, sometimes discontinuously, and can lead to difficulty in registering the XRFI scan maps with actual features on the sample.

The surface and detector angles also affect the penetration depth of the X-rays, and therefore the surface sensitivity of the measurement. From equation (3), we can find the mean depth at which the recorded fluorescent photons are generated,

$$
\begin{aligned}
\bar{d} &= \frac{\int_0^\infty \cos(\theta)\, s_i \exp\left[-(\mu_i + k\mu_f)\, s_i\right] ds_i}{\int_0^\infty \exp\left[-(\mu_i + k\mu_f)\, s_i\right] ds_i} \\
&= \frac{\cos\theta}{\mu_i + \mu_f(\cos\alpha + \tan\theta\sin\alpha)^{-1}}.
\end{aligned} \tag{6}
$$

Fig. 4 shows the variation in mean depth $\bar{d}$ with angle in a calcite sample. This effect further complicates analysis of XRFI data from samples with relief.
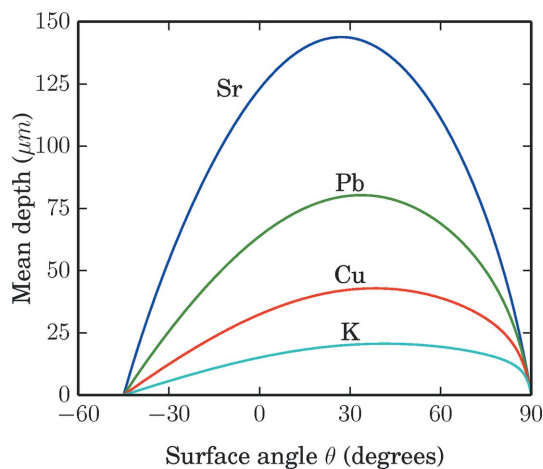

Figure 4
Mean depth from which detected fluorescent photons originate, for the K-$K_{\alpha 1}$, Cu-$K_{\alpha 1}$, Pb-$L_{\alpha 1}$ and Sr-$K_{\alpha 1}$ lines, in a CaCO$_3$ matrix, with incident beam energy 17 keV and detector angle $\alpha = 45°$.

3. Correction of XRFI maps for the effects of surface relief

If the approximate matrix of a sample is known and is spatially uniform, and the non-matrix elements are present in trace concentrations, then good approximations to $\mu(E)$ can be calculated. In that case the only undetermined variable in equation (5) is θ. Therefore, if $\theta(x, z)$ (where x, z are coordinates on the sample surface) can be determined, the XRFI data can be corrected for surface relief, at least to the extent that the approximations leading to equation (5) hold.

The most straightforward way to find $\theta(x, z)$ is to spatially profile the surface of the object, *e.g.* with a laser displacement sensor or *via* stereo photogrammetry. The three-dimensional profile must then be registered with the XRFI data. Profiling may not always be feasible due to equipment and time constraints.

This raises the question: is it possible to correct for angle based on the fluorescence data alone? Often, the matrix of a sample contains one XRF-visible element that is present in roughly uniform and high concentration over the entire surface; for instance, calcium in marble, limestone or gypsum. In this case we can assume that the reference element is, in fact, uniformly distributed, and use the intensity of one of its fluorescence lines to invert equation (5) and find $\theta(x, z)$. Equation (5) can then be used to correct the XRFI maps for each trace element.

We have found the following inversion and correction procedure to be effective:

(i) Given the matrix composition, compute the absorption coefficient $\mu(E)$ for the energy range of interest. We use the data of Brunetti *et al.* (2004) and Schoonjans *et al.* (2011).

(ii) Choose a single fluorescence peak from the fitted spectra, for a major matrix element that is expected to be uniformly distributed (*e.g.* Ca-K_α for limestone, marble and gypsum).

(iii) Let $I(x, z)$ be the intensity (*i.e.* number of counts) of this peak at points x, z in the scan; I_0 the median of I in a relatively flat region of the sample; and k_0 the geometric constant [according to equation (4)] for this region.

(iv) Compute

$$
\begin{aligned}
\gamma_0 &= I_0(\mu_i + k_0\mu_f), \\
k(x, z) &= \left[\gamma_0/I(x, y) - \mu_i\right]/\mu_f.
\end{aligned} \tag{7}
$$

(v) Invert equation (4) to find θ.

Next, with $k(x, z)$ determined by (7), calculate a correction factor as a function of the energy E of the fluorescence,

$$
C(E, x, z) = \frac{\mu_i + k(x, z)\mu(E)}{\mu_i + k_0\mu(E)}. \tag{8}
$$

Finally, apply this correction to the XRF spectrum at each pixel of the scan, re-fit the peaks in the corrected spectra, and then generate corrected XRFI maps for each element of interest.

4. Application to an incised tablet

As an example of the application of the above inversion and correction procedure, we examined a gypsum ($CaSO_4 \cdot 2H_2O$) tablet from what is now Iraq, dated *ca* 1000 BCE, shown in Fig. 5. The tablet is deeply incised with cuneiform figures. XRFI measurements were performed at beamline F3 of the Cornell High Energy Synchrotron Source (CHESS), using an incident X-ray beam energy of 17.0 keV, an X-ray beam size of 200 μm square, a stage angle of 90° and a detector angle of 45°. The detector was a four-element Vortex ME4 silicon drift detector from SII Nanotechnology. The sample stage was continuously scanned at 2 mm s^{-1}, and spectra determined for steps (pixels) of size 200 μm. Fluorescence spectra were fit using the PyMCA software library (Solé *et al.*, 2007). Fig. 6 shows the uncorrected Ca-K_α and Pb-L_α fluorescence maps for the outlined scan region in Fig. 5.

Calcium should be roughly uniformly distributed throughout the tablet, but the Ca map shows pronounced intensity variations that correlate with variations in surface angle. The detector was located to the right of the image, leading to apparently enhanced calcium fluorescence from the left-hand sides of the incisions.

The Pb map appears to indicate larger Pb concentrations in the incisions. However, it is not clear whether this is a geometric artifact since, like Ca, Pb fluorescence is stronger on the left-hand sides of the incisions. This tablet illustrates typical complications in interpreting fluorescence maps from non-planar objects.

Applying the inversion procedure outlined above and using the Ca-K_α peak at 3.69 keV as the reference peak yields the map of surface orientation angle θ shown at the top of Fig. 7. Fig. 7, bottom left, shows a rendering of the surface with angles as shown at the top, shaded as if illuminated by a light from the approximate position of the detector; the luminance L was computed using Lambertian shading, with $L \propto \cos(\alpha - \theta)$. Interestingly, this shows the pattern of relief more clearly than the optical photograph shown at the bottom right;

Figure 5
Photograph of a deeply incised gypsum tablet dated *ca* 1000 BCE from what is now Iraq (Harvard Semitic Museum No. 1897.1.1), with the scan region examined in Figs. 6 through 8 outlined in black. The image has been adjusted to enhance brightness and contrast.
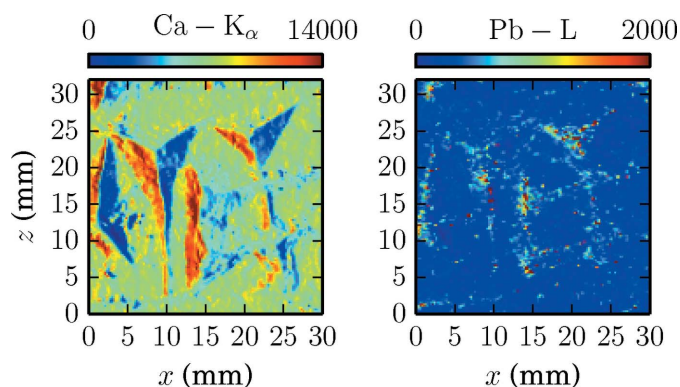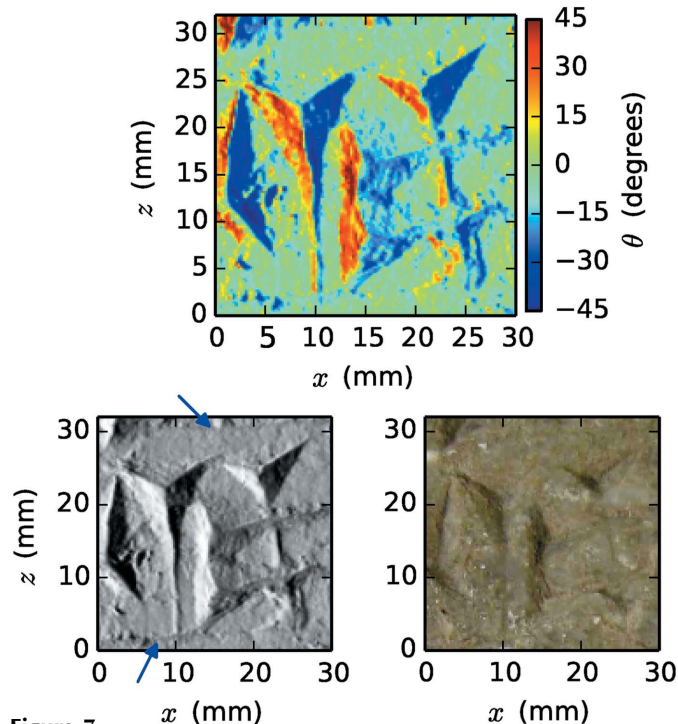

Figure 6
Uncorrected Ca-K_α and Pb-L fluorescence maps for the tablet in Fig. 5. Ca is expected to be roughly uniformly distributed within the tablet, but the Ca fluorescence intensity shows large variations, especially in incised regions, due to variations in surface orientation. The same effect complicates the interpretation of the map for Pb, a trace element whose concentration might be expected to correlate with incision. Scan taken with detector angle $\alpha = 45°$, stage angle $\theta_0 = 0°$, beam energy $E_i = 17.0$ keV, beam size 300 μm and step size 250 μm.

Figure 7
Top: map of surface angle θ computed from the Ca-K_α fluorescence map of Fig. 6. Bottom left: rendering of surface of the scanned area, computed from the surface angle map above and shaded as if obliquely illuminated from the right-hand side by a light source. The reconstruction gives a clear and detailed picture of the surface relief, including the fine horizontal rulings at the top and bottom (marked by arrows). Bottom right: photograph of the scanned area, adjusted to enhance contrast and brightness.

it is surprisingly accurate, considering the restrictive approximations under which it was computed. Note that, while the fluorescence intensity gives no direct information about φ rotations of the local surface normal (out of the xy plane), only $\theta(x, z)$ is needed to reconstruct the surface topography.

Using the surface orientation map in Fig. 7, the XRFI maps can now be corrected. We first check the corrected Ca-K_β map (4.01 keV) map. The Ca-K_β peak was measured and fitted independently of the Ca-K_α peak, so, if our model is valid, the corrected Ca-K_β map shown at the upper left in Fig. 8 should be almost flat. Indeed, it is, aside from small regions where the surface was at an angle $\theta < -\alpha = -45°$ and so was blocked from the detector's view.

Fig. 8 also shows corrected Pb and Ti fluorescence maps. In contrast to Fig. 6, Pb now appears evenly distributed between the left and right sides of the incisions. We are confident, therefore, that there actually is an increased concentration of Pb (and also Ti) within the incised features. These trace elements could have been introduced from the tools used to carve the figures [titanium has been associated with bronze-age tin production (Adriaens, 1996)], paint used to decorate the tablet, or contaminants which, for example, have been scrubbed from the field of the tablet but not from the protected valleys.

We emphasize that in calculating the corrections we have assumed that the sample composition normal to the average surface plane is uniform within the X-ray attenuation length (roughly 600 µm). In the limiting case where all trace elements were concentrated within a very thin surface layer (*i.e.* much thinner than the attenuation length), there would be a smaller correction to the trace element concentrations, proportional to $1/\cos\gamma$ (where γ is the angle between the surface normal and $-\mathbf{b}$), given by $\cos\gamma = -\mathbf{b}\cdot\mathbf{n}$. Applying this latter correction produced maps that were qualitatively similar to the uncorrected ones. In either case, there is evidently an increased concentration of Pb and Ti in the incisions.

Also note that our correction procedure assumes that elements of interest do not affect the detected fluorescence from the matrix reference element. For example, a thick Pb surface layer (*e.g.* from a pigment) would absorb and therefore mask the Ca fluorescence that we use as a reference, and equation (7) would then underestimate the surface angle. For the specimen considered here, there is no visual or XRF evidence of such layers; the elements of interest are present in trace concentrations.

5. Conclusions

We have derived simple expressions for the modulation of X-ray fluorescence intensity by surface orientation relative to the incident beam, and we have demonstrated a correction procedure applicable to trace element maps of such samples. The analysis assumes that the major elemental constituents of the matrix are homogeneous throughout the sample, that the surface is locally flat on the scale of the X-ray beam, and that absorption of matrix element fluorescence by trace element layers can be neglected. These assumptions should be approximately valid for a wide range of samples.

A key advantage of this method is its simplicity, both in the requisite experimental apparatus (a single detector, and no separate apparatus for determining surface topography) and in its analysis. However, the estimates of surface angles might be improved by using multiple detectors, *e.g.* positioned in pairs on opposite sides of the beam. One approach to dual-detector topography correction was reported by Smilgies *et al.* (2012). However, that work simply used the sum and difference of the maps from the two detectors, and, as equation (5) shows, the variation of fluorescence intensity with angle is not linear, even in the case of a flat homogeneous surface. Fitting equation (7) to fluorescence maps from multiple detectors would likely yield better corrections, and would reduce the occurrence of 'blind spots' where the detector's view is blocked by another part of the sample. Finally, the recently developed highly parallel annular detectors (Ryan *et al.*, 2010) raise an intriguing possibility: analyzed using methods similar to those outlined here, a single scan might provide extremely detailed reconstructions of both the composition and geometry of a sample.
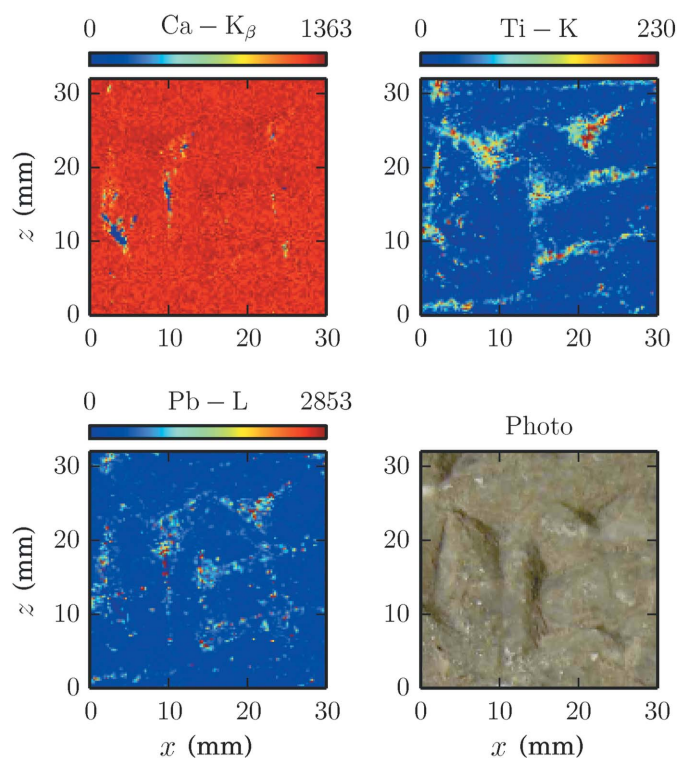
Figure 8
Angle-corrected fluorescence maps for Ca-K_β, Pb-L and Ti-K. As expected, the Ca map is almost uniform (except where the angle exceeds $-45°$). The corrected Pb and Ti maps show an increased concentration of these elements in the incised areas.

collaboration on imaging Greek and Latin inscriptions on stone that led to the present work. This work was supported in part by grants from the Samuel H. Kress Foundation and the Mellon Foundation. ECG also acknowledges support from the National Science Foundation under grant DMR-0805240.

References

Adriaens, A. (1996). *Microchim. Acta*, **124**, 89–98.

Bergmann, U. & Knox, K. T. (2009). *Proc. SPIE*, **7247**, 724702.

Bonizzoni, L., Maloni, A. & Milazzo, M. (2006). *X-ray Spectrom.* **35**, 390–399.

Brunetti, A., Sanchez del Rio, M., Golosio, B., Simionovici, A. & Somogyi, A. (2004). *Spectrochim. Acta B*, **59**, 1725–1731.

Dik, J., Janssens, K., Snickt, G. V. D., van der Loeff, L., Rickers, K. & Cotte, M. (2008). *Anal. Chem.* **80**, 6436–6442.

Dzubay, T. G., Jarrett, B. V. & Jaklevic, J. M. (1974). *Nucl. Instrum. Methods*, **115**, 297–299.

Limburg, K. E., Huang, R. & Bilderback, D. H. (2007). *X-ray Spectrom.* **36**, 336–342.

Lintern, M., Anand, R., Ryan, C. & Paterson, D. (2013). *Nat. Commun.* **4**, 2274.

Mantler, M. & Schreiner, M. (2000). *X-ray Spectrom.* **29**, 3–17.

Powers, J., Dimitrova, N., Huang, R., Smilgies, D.-M., Bilderback, D. H. & Thorne, R. E. (2005). *Z. Papyrol. Epigr.* **152**, 221–227.

Powers, J., Smilgies, D.-M., Geil, E. C., Clinton, K., Peachin, M. & Thorne, R. E. (2009). *J. Archaeol. Sci.* **36**, 343–350.

Rivers, M. L., Sutton, S. R. & Jones, K. W. (1992). *X-ray Microscopy III*, edited by A. G. Michette, G. R. Morrison and C. J. Buckley, Vol. 67 of *Springer Series in Optical Sciences*, pp. 212–216. Berlin: Springer.

Ryan, C. G., Siddons, D. P., Kirkham, R., Dunn, P. A., Kuczewski, A., Moorhead, G., De Geronimo, G., Paterson, D. J., de Jonge, M. D., Hough, R. M., Lintern, M. J., Howard, D. L., Kappen, P. & Cleverley, J. (2010). *AIP Conf. Proc.* **1221**, 9–17.

Schoonjans, T., Brunetti, A., Golosio, B., del Rio, M. S., Solé, V., Ferrero, C. & Laszlo, V. (2011). *Spectrochim. Acta B*, **66**, 776–784.

Scot, V., Fermandez, J. E., Vincze, L. & Janssens, K. (2007). *Nucl. Instrum. Methods Phys. Res. B*, **263**, 204–208.

Smilgies, D.-M., Powers, J. A., Bilderback, D. H. & Thorne, R. E. (2012). *J. Synchrotron Rad.* **19**, 547–550.

Solé, V., Papillon, E., Cotte, M., Walter, P. & Susini, J. (2007). *Spectrochim. Acta B*, **62**, 63–68.

Trojek, T. (2011). *J. Anal. At. Spectrom.* **26**, 1253–1257.

Trojek, T. (2012). *Appl. Radiat. Isotopes*, **70**, 1206–1209.

Trojek, T., Čecàk, T. & Musílek, L. (2010). *Nucl. Instrum. Methods Phys. Res. A*, **619**, 266–269.

Trojek, T. & Wegrzynek, D. (2010). *Nucl. Instrum. Methods Phys. Res. A*, **619**, 311–315.

Urbach, H. P. & de Bokx, P. K. (2001). *Phys. Rev. B*, **63**, 085408.